Journal of Computational and Applied Mathematics 295 (2016) 13–24

Contents lists available at ScienceDirect

Journal of Computational and Applied Mathematics

journal homepage: www.elsevier.com/locate/cam

Simulation of cardiac perfusion by contrast in the myocardium using a formulation of flow in porous media

J.R. Alves, R.A.B. de Queiroz, R.W. dos Santos *

Graduate Program in Computational Modeling, Federal University of Juiz de Fora, 36036-900, Juiz de Fora, MG, Brazil

ARTICLE INFO

Article history:
Received 2 October 2014
Received in revised form 30 March 2015

Keywords:
Computational modeling
Porous media
Myocardial perfusion
Contrast enhanced MRI

ABSTRACT

This paper presents a computational model that characterizes the spatio-temporal dynamics of blood perfusion in cardiac myocardium. Specifically, we are interested in reproducing qualitative images obtained by contrast-enhanced exams, which are widely used in clinical medicine to evaluate the blood perfusion in the heart. The application of contrast allows the detection of injuries, ischemic regions, fibrosis or tumors. Here we focus on the pathological case associated to subendocardial infarct. In our modeling, we will consider the tissue of cardiac myocardium as a porous media, i.e. a solid region with empty spaces. To this end, the modeling was based on differential equations and Darcy's Law, which correlates tissue permeability, pressure difference and the blood flow in the cardiac tissue.

1. Introduction

Cardiac perfusion is the mechanism by which the heart is supplied with oxygen and nutrients. Numerical simulations of this perfusion allow quantitative and qualitative analysis (we will focus on the second) and support the understanding of important aspects in blood flow dynamics. In addition, computational models can improve diagnostics and treatments. However, the simulation of cardiac perfusion is a challenge. In previous works [1,2] blood perfusion was modeled considering the myocardium as a porous media. In some of these previous works [1] a multi-compartment model was proposed to take into account the differences between the sizes or diameters of blood vessels. Nevertheless, all the mentioned models were based on differential equations and Darcy's Law, and focused on the simulation of pressure and blood flow distributions in the cardiac tissue.

Nowadays, neither pressure nor blood flow distributions in the cardiac tissue can be acquired non-invasively. However, the injection of contrasts during clinical exams based on imaging, such as Magnetic Resonance Imaging (MRI) or Computerized Tomography (CT), allows the non-invasive detection of ischemic regions, fibrosis or tumors.

For instance, in cardiac perfusion MRI [3], a chemical contrast, usually based in gadolinium, is injected in the patient. After the injection, different images at different times are obtained for the same heart region and at the same heart phase, i.e. at a particular instant with respect to cardiac contraction (triggered via the R-wave of a real-time Electrocardiogram). With this temporal series of images, the clinician can observe how contrast perfuses the cardiac tissue, since image brightness (near to white) is highly correlated to the presence of contrast. Therefore, if the blood perfuses the myocardium optimally, after some cardiac contractions (captured by MRI), cardiac tissue in the acquired images shines homogeneously white. If, however, some regions of the heart are not accordingly perfused, darker (near black) spots will appear in some of the images.

In this work the same framework is used as in [2] (a single-compartment approach) to model pressure and blood flow distributions. However, to focus in the simulation of contrast based perfusion we add a new variable of interest in our model:

* Corresponding author. Tel.: +55 3288281099.
E-mail address: rodrigo.weber@ufjf.edu.br (R.W. dos Santos).

http://dx.doi.org/10.1016/j.cam.2015.04.008
0377-0427/

the spatio-temporal dynamics of contrast concentration in the cardiac tissue. To this end a new differential equation was coupled to the mathematical model that captures the pressure distribution. This new equation considers both advection (due to blood pressure gradients) and diffusion terms, i.e. it is an advection–diffusion partial differential equation (PDE). This new system of partial differential equations is discretized by the Finite Volume Method (FVM).

We have simulated two different scenarios: the contrast perfusion of a normal cardiac tissue and of one with a subendocardial infarct. The simulation results are qualitatively in agreement with the expected phenomena, i.e. with the described images obtained by non-invasive exams of cardiac perfusion MRI [3].

2. Mathematical model

In this section, we describe the coupled system of PDEs that models both pressure distribution and the spatio-temporal dynamics of contrast in the heart. Our model takes into account some important simplifications in our hypothesis. First, the heart is considered to be in a rigid configuration, i.e. it is not contracting or deforming along time. Indeed, most of the perfusion in the heart takes place during the diastole phase (relaxed configuration), since during systole (contraction) the arteries inside the cardiac tissue are subject to high pressures that prevail blood flow or perfusion. Therefore, the available time-window for cardiac perfusion is around 0.5 s as described in [2]. In addition, for the specific goal of reproducing contrast-based perfusion MRI exams, the non-contracting hypothesis is also valid. As mentioned before, after injection of contrast, different images at different times are obtained for the same heart region but always at the same heart phase, i.e. at a particular instant with respect to cardiac contraction (triggered via the R-wave of a real-time Electrocardiogram). We also consider cardiac tissue to be incompressible during this particular phase of diastole [1]. Finally, in this first model of the dynamics of contrast in the heart we consider cardiac tissue as a porous medium, with flow taking place only in the intravascular region of cardiac tissue. This same hypothesis was used in [1]. However, as it will be pointed out by our results this last hypothesis turned out to be the main limitation of this work, since gadolinium also perfuses in part of the extravascular region, i.e. in the interstitial space that exists between cardiac myocytes. Finally, in our model we also considered the existence of a preferred direction for cardiac perfusion. This direction would follow the well known distribution of cardiac fibers in the heart.

2.1. The model for pressure distribution

Next we consider the heart as a porous and incompressible media. For this case, applying classical Darcy's formulation gives us:

$$\nabla \cdot \vec{v} = s, \quad \text{in } \Omega \tag{1}$$

$$\vec{v} = -\mathbf{K}\nabla p, \quad \text{in } \Omega \tag{2}$$

where $\mathbf{K} = \begin{pmatrix} K_x & K_{xy} \\ K_{xy} & K_y \end{pmatrix}$ is thepermeability tensor, i.e. we consider the permeability to be anisotropic and to follow the cardiac myocyte distribution; p is the pressure; s is a source/sink term; $\vec{v}$ is the Darcy velocity and Ω is the domain. Here we consider $s = 0$. Substituting Eq. (2) in Eq. (1), we obtain:

$$\nabla \cdot \mathbf{K}\nabla p = 0, \quad \text{in } \Omega. \tag{3}$$

The boundary conditions for Eq. (3), which is written in terms of pressure, are given by Dirichlet and Neumann, respectively:

$$p = p_k \quad \text{in } \Gamma_D \tag{4}$$

$$-\mathbf{K}\nabla p \cdot \vec{\mathbf{n}} = \alpha_p \quad \text{in } \Gamma_N \tag{5}$$

where $\vec{\mathbf{n}}$ is the normal vector.

2.2. Modeling the contrast dynamics as a single-phase flow

Consider the mass-balance equation:

$$\frac{\partial(\phi C)}{\partial t} + \nabla \cdot \vec{J} - Q = 0 \tag{6}$$

where C is the concentration of the contrast in the tissue, ϕ is the medium porosity and Q is a source term. We assume that no reaction takes place at the considered time-scale and that the flux $\vec{J}$ has two components, one advective ($\vec{v}C$) and the other diffusive ($-D\nabla C$):

$$\vec{J} = \vec{v}C - D\nabla C \tag{7}$$

where $\boldsymbol{D} = \begin{pmatrix} d_x & d_{xy} \\ d_{xy} & d_y \end{pmatrix}$ is thediffusion tensor that is also taken as anisotropic. Thus, rewriting (6), we have:

$$\frac{\partial \phi C}{\partial t} + \nabla \cdot \vec{v}C - \nabla \cdot (\boldsymbol{D}\nabla C) = 0. \tag{8}$$

Again, we use the Neumann and Dirichlet boundary conditions:

$$C = \beta \quad \text{in } \Gamma_D \tag{9}$$

$$\mathbf{D}\nabla C \cdot \vec{\mathbf{n}} = \gamma \quad \text{in } \Gamma_N \tag{10}$$

where $\vec{\mathbf{n}}$ is the normal vector. As initial condition, we have:

$$C(x, 0) = C_0(x) \quad \text{in } \Omega. \tag{11}$$

Rewriting the whole problem:

For a porous domain Ω with boundary $\partial\Omega = \Gamma_D \cup \Gamma_N$ in the time interval $I = (0, T]$, given the permeability $\mathbf{K} : \Omega \to \Re^2 \times \Re^2$ and diffusion tensors $\mathbf{D} : \Omega \to \Re^2 \times \Re^2$, the porosity ϕ, the boundary conditions $p_K, \beta : \Gamma_D \to \Re$, the normal fluxes on the boundary $\alpha_p, \gamma : \Gamma_N \to \Re$ and the initial condition $C_o : \Omega \to \Re^2$, find the concentration $C : \Omega \times I \to \Re$ and the pressure $p : \Omega \to \Re$ that satisfy:

$$\nabla \cdot \mathbf{K}\nabla p = 0, \quad \text{in } \Omega \tag{12}$$

$$\frac{\partial \phi C}{\partial t} + \nabla \cdot \vec{v}C - \nabla \cdot (\boldsymbol{D}\nabla C) = 0, \quad \text{in } \Omega \tag{13}$$

$$p = p_k, \quad \text{in } \Gamma_D \tag{14}$$

$$-\mathbf{K}\nabla p \cdot \vec{\mathbf{n}} = \alpha_p \quad \text{in } \Gamma_N \tag{15}$$

$$C = \beta, \quad \text{in } \Gamma_D \tag{16}$$

$$\mathbf{D}\nabla C \cdot \vec{\mathbf{n}} = \gamma \quad \text{in } \Gamma_N \tag{17}$$

$$C(x, 0) = C_0(x) \quad \text{in } \Omega \tag{18}$$

where $\vec{\mathbf{n}}$ is the normal vector in the boundary $\partial\Omega$. Γ_D and Γ_N are, respectively, the parts of the boundary with prescribed concentration (Dirichlet condition) and prescribed flux (Neumann condition).

3. Numerical methods

For the discretization, the FVM formulation was used, which consists in the evaluation of influx and outflux of a control volume around each node of the mesh. The FVM applied to Eq. (3) (an elliptic PDE) gives us a linear system with one equation for each node. The control volumes were taken as squares of size equal to h. This system was solved by the iterative method of Jacobi, with a error tolerance (stop criteria) set to 10^{-8}. The discretized equation of pressure using this method in each node is:

$$\begin{aligned} p_{i,j} = \Big[& \left(4Tx_{i+\frac{1}{2},j} + Txy_{i,j+\frac{1}{2}} - Txy_{i,j-\frac{1}{2}}\right) \cdot p_{i+1,j} + \left(4Tx_{i-\frac{1}{2},j} - Txy_{i,j+\frac{1}{2}} + Txy_{i,j-\frac{1}{2}}\right) \cdot p_{i-1,j} \\ & + \left(4Ty_{i,j+\frac{1}{2}} + Txy_{i+\frac{1}{2},j} - Txy_{i-\frac{1}{2},j}\right) \cdot p_{i,j+1} + \left(4Ty_{i,j-\frac{1}{2}} - Txy_{i+\frac{1}{2},j} + Txy_{i-\frac{1}{2},j}\right) \cdot p_{i,j-1} \\ & + \left(Txy_{i+\frac{1}{2},j} + Txy_{i,j+\frac{1}{2}}\right) \cdot p_{i+1,j+1} + \left(Txy_{i-\frac{1}{2},j} + Txy_{i,j+\frac{1}{2}}\right) \cdot p_{i-1,j-1} - \left(Txy_{i+\frac{1}{2},j} + Txy_{i,j-\frac{1}{2}}\right) \cdot p_{i+1,j-1} \\ & - \left(Txy_{i-\frac{1}{2},j} + Txy_{i,j+\frac{1}{2}}\right) \cdot p_{i-1,j+1} \Big] / 4 \cdot \left(Tx_{i+\frac{1}{2},j} + Tx_{i-\frac{1}{2},j} + Tx_{i,j+\frac{1}{2}} + Tx_{i,j-\frac{1}{2}}\right) \end{aligned} \tag{19}$$

where

$$\begin{aligned} Tx_{i+\frac{1}{2},j} &= 2\frac{Kx_{i+1,j} \cdot Kx_{i,j}}{Kx_{i+1,j} + Kx_{i,j}}, \\ Tx_{i-\frac{1}{2},j} &= 2\frac{Kx_{i,j} \cdot Kx_{i-1,j}}{Kx_{i,j} + Kx_{i-1,j}}, \\ Ty_{i,j+\frac{1}{2}} &= 2\frac{Ky_{i,j+1} \cdot Ky_{i,j}}{Ky_{i,j+1} + Ky_{i,j}}, \\ Ty_{i,j-\frac{1}{2}} &= 2\frac{Ky_{i,j-1} \cdot Ky_{i,j}}{Ky_{i,j-1} + Ky_{i,j}}, \\ Txy_{i+\frac{1}{2},j} &= 2\frac{Kxy_{i+1,j} \cdot Kxy_{i,j}}{Kxy_{i+1,j} + Kxy_{i,j}}, \\ Txy_{i-\frac{1}{2},j} &= 2\frac{Kxy_{i,j} \cdot Kxy_{i-1,j}}{Kxy_{i,j} + Kxy_{i-1,j}}, \\ Txy_{i,j+\frac{1}{2}} &= 2\frac{Kxy_{i,j+1} \cdot Kxy_{i,j}}{Kxy_{i,j+1} + Kxy_{i,j}}, \end{aligned} \tag{20}$$

$$Txy_{i,j-\frac{1}{2}} = 2\frac{Kxy_{i,j-1}\cdot Kxy_{i,j}}{Kxy_{i,j-1}+Kxy_{i,j}},$$

are the transmissibilities in the faces of control volume around each node. Once the pressure field is known it is used in Eq. (2) to obtain the velocity in the faces of the control volume by:

$$\begin{aligned}
v_{i+\frac{1}{2},j} &= -Tx_{i+\frac{1}{2},j}\cdot\left(\frac{p_{i+1,j}-p_{i,j}}{h}\right) - Txy_{i+\frac{1}{2},j}\cdot\left(\frac{p_{i,j+1}+p_{i+1,j+1}-p_{i,j-1}-p_{i+1,j-1}}{4\cdot h}\right)\\
v_{i-\frac{1}{2},j} &= -Tx_{i-\frac{1}{2},j}\cdot\left(\frac{p_{i,j}-p_{i-1,j}}{h}\right) - Txy_{i-\frac{1}{2},j}\cdot\left(\frac{p_{i-1,j+1}+p_{i,j+1}-p_{i-1,j-1}-p_{i,j-1}}{4\cdot h}\right)\\
v_{i,j+\frac{1}{2}} &= -Tx_{i,j+\frac{1}{2}}\cdot\left(\frac{p_{i,j+1}-p_{i,j}}{h}\right) - Txy_{i+\frac{1}{2},j}\cdot\left(\frac{p_{i+1,j+1}+p_{i+1,j}-p_{i-1,j+1}+p_{i-1,j}}{4\cdot h}\right)\\
v_{i,j-\frac{1}{2}} &= -Tx_{i,j-\frac{1}{2}}\cdot\left(\frac{p_{i,j}-p_{i,j-1}}{h}\right) - Txy_{i+\frac{1}{2},j}\cdot\left(\frac{p_{i+1,j}+p_{i+1,j-1}-p_{i-1,j}+p_{i-1,j-1}}{4\cdot h}\right).
\end{aligned} \tag{21}$$

The velocity is used in the second term of the left side in Eq. (8), which is discretized as

$$\phi\cdot\frac{(C_{i,j}^{n+1}-C_{i,j}^{n})}{\Delta t} = dif_{i,j}^{n} - adv_{i,j}^{n}$$

where $C_{i,j}^{n}$ is the discretization of $C(n\Delta t, ih, jh)$, with time step, Δt, and space discretization, h.

The discretization of the diffusive term $dif_{i,j}^{n}$ follows that of the pressure equation, Eq. (19), substituting p for C, and substituting the transmissibilities described in Eq. (20) by harmonic averages of the diffusion tensor D.

The advective term is given by

$$adv_{i,j}^{n} = \left[v_{i+\frac{1}{2},j}\cdot C_{i+\frac{1}{2},j} - v_{i-\frac{1}{2},j}\cdot C_{i-\frac{1}{2},j} + v_{i,j+\frac{1}{2}}\cdot C_{i,j+\frac{1}{2}} - v_{i,j-\frac{1}{2}}\cdot C_{i,j-\frac{1}{2}}\right]/h. \tag{22}$$

For the numerical approximation of this term (advective), we implemented and compared two different schemes: the first-order upwind scheme (FOU) and the third-order polynomial upwind scheme (TOPUS) [4–6]. The next subsection presents further details of these two methods.

3.1. Numerical approximation of the advective term

The success in obtaining acceptable numerical simulations (accurate and free of oscillations and over smoothing) for transport problems involving advection and diffusion is one of the most interesting and challenging themes in the area of computational fluid dynamics, and has attracted many researchers in recent years. For the diffusive term, the central differences scheme works very well, without any major problems. But for the advective term it is necessary to make the decision of which scheme must be used to ensure accuracy and convergence of the numerical method. In this section, we present the discretization of the convective term in Eq. (22) via the FOU and TOPUS schemes.

To complete the discretization, FOU and TOPUS schemes are used to estimate the values $C_{i+\frac{1}{2},j}$, $C_{i-\frac{1}{2},j}$, $C_{i,j+\frac{1}{2}}$ and $C_{i,j-\frac{1}{2}}$ of Eq. (22). In what follows, we interchange the notations for the velocities normal to the faces of a control volume: $v_{i+\frac{1}{2},j} = u_f$, $v_{i-\frac{1}{2},j} = u_g$, $v_{i,j+\frac{1}{2}} = v_m$ and $v_{i,j-\frac{1}{2}} = v_n$.

3.1.1. FOU scheme

The traditional FOU scheme estimates the values of $C_{i+\frac{1}{2},j}$, $C_{i-\frac{1}{2},j}$, $C_{i,j+\frac{1}{2}}$ e $C_{i,j-\frac{1}{2}}$ by using the information of the direction of propagation. Therefore:

- when $u_f \geq 0$

  $C_{i+\frac{1}{2},j} = C_{i,j}$;
- when $u_f < 0$

  $C_{i+\frac{1}{2},j} = C_{i+1,j}$;
- when $u_g \geq 0$

  $C_{i-\frac{1}{2},j} = C_{i-1,j}$;
- when $u_g < 0$

  $C_{i-\frac{1}{2},j} = C_{i,j}$;

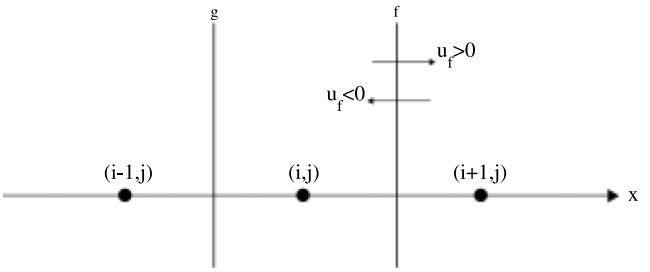

Fig. 1. Approximation of C_f in $f = (i + \frac{1}{2}, j)$.

- when $v_m \geq 0$

$$C_{i,j+\frac{1}{2}} = C_{i,j}; \tag{23}$$

- when $v_m < 0$

$$C_{i,j+\frac{1}{2}} = C_{i,j+1}; \tag{24}$$

- when $v_n \geq 0$

$$C_{i,j-\frac{1}{2}} = C_{i,j-1}; \tag{25}$$

- when $v_n < 0$

$$C_{i,j-\frac{1}{2}} = C_{i,j}. \tag{26}$$

3.1.2. TOPUS scheme

As a high order method, the TOPUS scheme uses a wider stencil (3 neighboring points) for the approximation of each of the values $C_{i+\frac{1}{2},j}$, $C_{i-\frac{1}{2},j}$, $C_{i,j+\frac{1}{2}}$ and $C_{i,j-\frac{1}{2}}$. The approximations for C at the surfaces are obtained using the neighboring points D (*Downstream*), R (*Remote-Upstream*) and U (*Upstream*) of the point $P = (i, j)$ where one needs to approximate the advective term. As an Upwind scheme, these points are also defined according to the direction of propagation, i.e. according to the signals of u_f, u_g, v_m, v_n. Therefore, we have the following rules and equations that define the TOPUS scheme:

1. Approximation to $C_{i+\frac{1}{2},j}$ at face f (see computational stencil in Fig. 1)
   - When $u_f \geq 0$; in this case positions D, R and U assume, respectively, the values $D = (i + 1, j)$, $R = (i - 1, j)$ and $U = (i, j)$. The value $C_{i+\frac{1}{2},j}$, using the TOPUS scheme is obtained as:

$$C_{i+\frac{1}{2},j} = \begin{cases} C_{i-1,j} + (C_{i+1,j} - C_{i-1,j})(2\hat{C}_U^4 - 3\hat{C}_U^3 + 2\hat{C}_U), & \hat{C}_U \in [0, 1], \\ C_{i,j}, & \hat{C}_U \notin [0, 1], \end{cases}$$

   where

$$\hat{C}_U = \frac{C_{i,j} - C_{i-1,j}}{C_{i+1,j} - C_{i-1,j}}.$$

   - When $u_f < 0$: $D = (i, j)$, $R = (i + 2, j)$ and $U = (i + 1, j)$.

$$C_f = C_{i+\frac{1}{2},j} = \begin{cases} C_{i+2,j} + (C_{i,j} - C_{i+2,j})(2\hat{C}_U^4 - 3\hat{C}_U^3 + 2\hat{C}_U), & \hat{C}_U \in [0, 1], \\ C_{i+1,j}, & \hat{C}_U \notin [0, 1], \end{cases}$$

   where

$$\hat{C}_U = \frac{C_{i+1,j} - C_{i+2,j}}{C_{i,j} - C_{i+2,j}}.$$

2. Approximation to $C_{i-\frac{1}{2},j}$ at face g (see Fig. 2)
   - When $u_g \geq 0$; in this case the positions D, R and U assume, respectively, the values $D = (i, j)$, $R = (i - 2, j)$ and $U = (i - 1, j)$. The value $C_{i-\frac{1}{2},j}$, using the TOPUS scheme is approximated as:

$$C_g = C_{i-\frac{1}{2},j} = \begin{cases} C_{i-2,j} + (C_{i,j} - C_{i-2,j})(2\hat{C}_U^4 - 3\hat{C}_U^3 + 2\hat{C}_U), & \hat{C}_U \in [0, 1], \\ C_{i-1,j} & \hat{C}_U \notin [0, 1], \end{cases}$$

   where

$$\hat{C}_U = \frac{C_{i-1,j} - C_{i-2,j}}{C_{i,j} - C_{i-2,j}}.$$

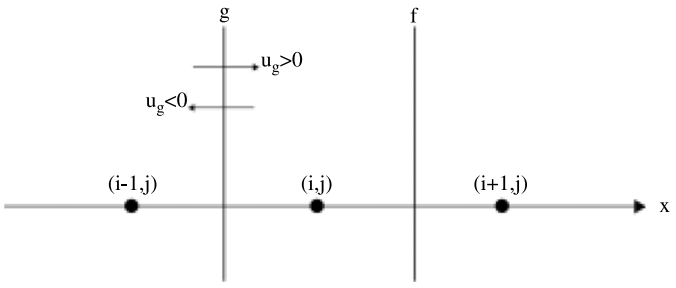

Fig. 2. Approximation of C_g in face $g = (i - \frac{1}{2}, j)$.

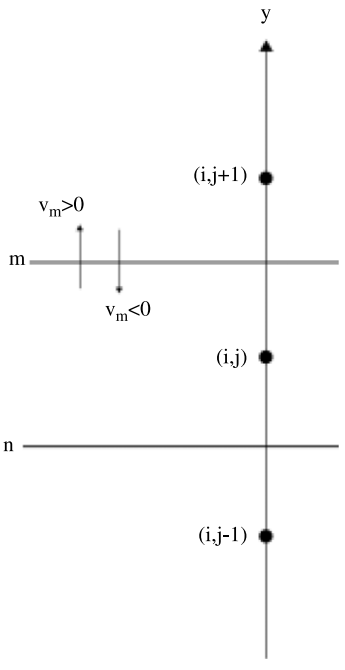

Fig. 3. Approximation of C_m in face $m = (i, j + \frac{1}{2})$.

- When $u_g < 0$; $D = (i - 1, j)$, $R = (i + 1, j)$ and $U = (i, j)$.

$$C_g = C_{i-\frac{1}{2},j} = \begin{cases} C_{i+1,j} + (C_{i-1,j} - C_{i+1,j})(2\hat{C}_U^4 - 3\hat{C}_U^3 + 2\hat{C_U}), & \hat{C}_U \in [0, 1], \\ C_{i,j} \quad \hat{C}_U \notin [0, 1], \end{cases}$$

where

$$\hat{C}_U = \frac{C_{i,j} - C_{i+1,j}}{C_{i-1,j} - C_{i+1,j}}.$$

3. Approximation to $C_{i,j+\frac{1}{2}}$ at face m (Fig. 3)

- When $v_m \geq 0$: $D = (i, j + 1)$, $R = (i, j - 1)$ and $U = (i, j)$.

$$C_{i,j+\frac{1}{2}} = \begin{cases} C_{i,j-1} + (C_{i,j+1} - C_{i,j-1})(2\hat{C}_U^4 - 3\hat{C}_U^3 + 2\hat{C_U}), & \hat{C}_U \in [0, 1], \\ C_{i,j}, \quad \hat{C}_U \notin [0, 1], \end{cases}$$

where

$$\hat{C}_U = \frac{C_{i,j} - C_{i,j-1}}{C_{i,j+1} - C_{i,j-1}}.$$

- When $v_m < 0$: $D = (i, j)$, $R = (i, j + 2)$ and $U = (i, j + 1)$.

$$C_{i,j+\frac{1}{2}} = \begin{cases} C_{i,j+2} + (C_{i,j} - C_{i,j+2})(2\hat{C}_U^4 - 3\hat{C}_U^3 + 2\hat{C_U}), & \hat{C}_U \in [0, 1], \\ C_{i,j+1}, \quad \hat{C}_U \notin [0, 1], \end{cases}$$

where

$$\hat{C}_U = \frac{C_{i,j+1} - C_{i,j+2}}{C_{i,j} - C_{i,j+2}}.$$

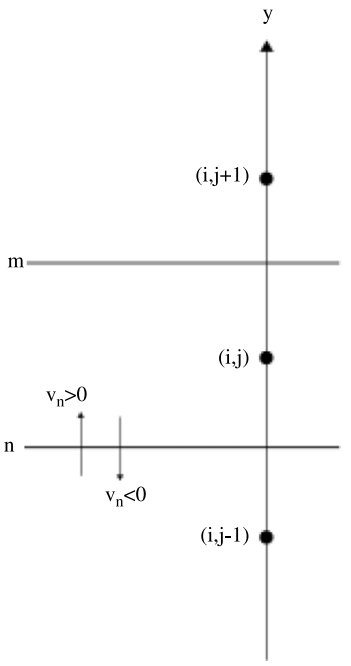

Fig. 4. Approximation of C_n in face $n = (i, j - \frac{1}{2})$.

4. Approximation to $C_{i,j-\frac{1}{2}}$ at face n (see Fig. 4)
   - When $v_n \geq 0$: $D = (i, j)$, $R = (i, j - 2)$ and $U = (i, j - 1)$.
   $$C_{i,j-\frac{1}{2}} = \begin{cases} C_{i,j-2} + (C_{i,j} - C_{i,j-2})(2\hat{C}_U^4 - 3\hat{C}_U^3 + 2\hat{C}_U), & \hat{C}_U \in [0, 1], \\ C_{i,j-1}, & \hat{C}_U \notin [0, 1], \end{cases}$$
   where
   $$\hat{C}_U = \frac{C_{i,j-1} - C_{i,j-2}}{C_{i,j} - C_{i,j-2}}.$$
   - When $v_n < 0$: $D = (i, j - 1)$, $R = (i, j + 1)$ and $U = (i, j)$.
   $$C_{i,j-\frac{1}{2}} = \begin{cases} C_{i,j+1} + (C_{i,j-1} - C_{i,j+1})(2\hat{C}_U^4 - 3\hat{C}_U^3 + 2\hat{C}_U), & \hat{C}_U \in [0, 1], \\ C_{i,j}, & \hat{C}_U \notin [0, 1], \end{cases}$$
   where
   $$\hat{C}_U = \frac{C_{i,j} - C_{i,j+1}}{C_{i,j-1} - C_{i,j+1}}.$$

   More details of the method can be found in [4–6].

4. Numerical experiments

The size of the transmural wall was set to 10 mm × 10 mm and it was discretized by a mesh of 100 × 100 nodes, corresponding to a slice covering the epicardium and endocardium (see Fig. 6). The prescribed pressures at epicardial and endocardial surfaces were set to be in the normal range as described before in [1]: $p(x, y) = 3.0$ kPa, $\forall (x, y) \in \Gamma_{west} \cup E1 \cup E3$ and $p(x, y) = 6.0$ kPa, $\forall (x, y) \in E2$. The pressure is higher in Γ_2 due to the fact that, for modeling the problem, we consider the presence of a coronary artery near this region (see Fig. 5). The porosity ϕ was assumed to be constant and equal to 0.10 [2].

Four different experiments were conducted: anisotropy and isotropy combined with non-infarcted and infarcted myocardium. For the simulations of isotropic and non-infarcted tissues we set $D = \begin{pmatrix} 0.5 \times 10^{-3} & 0 \\ 0 & 0.5 \times 10^{-3} \end{pmatrix}$ mm^2/s [7] and the permeability tensor was $K = \begin{pmatrix} 15.0 & 0 \\ 0 & 15.0 \end{pmatrix}$ mm^2/kPa s. To take into account the anisotropic nature of cardiac tissue we consider both the diffusion and the permeability tensor to follow the cardiac myocardial direction, which is known to be parallel to the endocardial and epicardial surfaces. Therefore, the diffusion tensor of gadolinium was set to $D = \begin{pmatrix} 0.1 \times 10^{-3} & 0 \\ 0 & 0.2 \times 10^{-3} \end{pmatrix}$ mm^2/s [7] and the permeability tensor was set to $K = \begin{pmatrix} 3.0 & 0 \\ 0 & 15.0 \end{pmatrix}$ mm^2/kPa s [1]. To simulate a subendocardial infarct, we changed D and K in a small rectangular region near the endocardial surface (see Fig. 5). In this region both the diffusion and permeability tensors were homogeneously reduced to αD and αK, respectively, with $\alpha = 0.1$.

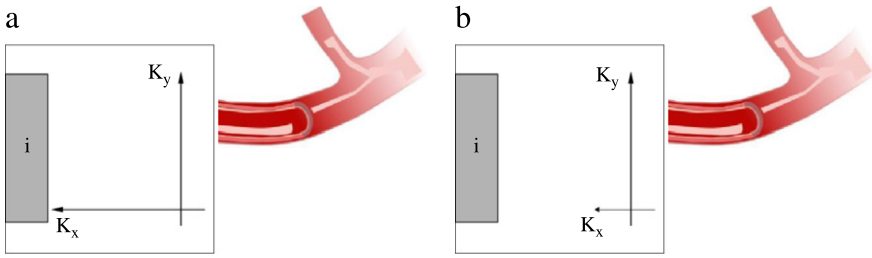

Fig. 5. Simulation of infarcted myocardium in the isotropic (a) and anisotropic (b) cases.

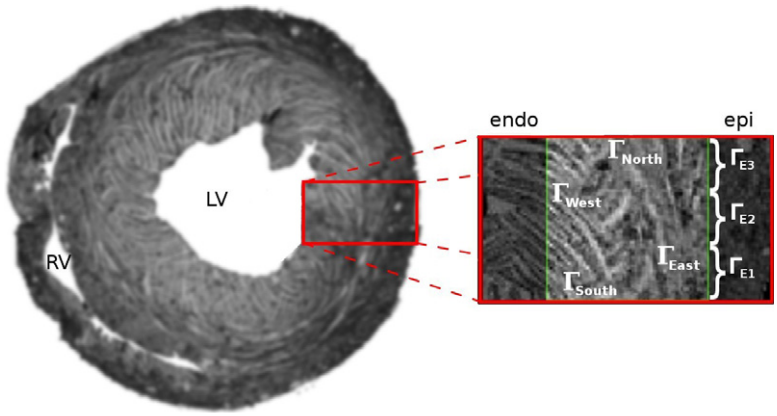

Fig. 6. Short axis of the heart (left) and a transmural region of the left ventrical (right) that comprises the simulation domain.

The simulation time in all cases was 0.55 s [2]. This is the time-window for cardiac perfusion during the diastole phase. We used the Explicit Euler method in the temporal part of the advection–diffusion equation. Therefore, our numerical method is conditionally stable, i.e., Δt (the time step) and h (the discretization step in both x and y directions) have to fulfill the following CFL conditions [8,9]:

$$\Delta t \leq \frac{2D_{\max}}{v_{\max}^2} \tag{27}$$

$$\Delta t \leq \frac{h^2}{4 \cdot D_{\max}}, \tag{28}$$

where $v_{\max}$ is the maximum norm of the velocity field and $D_{\max}$ is the maximum diffusion coefficient.

4.1. TOPUS vs. FOU

The method described above, TOPUS, is more accurate ($O(h^2)$) than the FOU ($O(h)$). More details of the method can be found in [4–6]. We compared both discretizations by performing a convergence analysis as follows: we considered the most refined mesh solved by FOU as the "reference solution". The other meshes, all of them solved by both the FOU and TOPUS schemes, are then compared to the "reference solution". The fine mesh was fixed with 257×257 points. The other meshes were:

- 17×17
- 33×33
- 65×65
- 129×129.

The scenario used for this convergence analysis was the one that considers both anisotropy and an infarcted region, as described before. We chose the time instant of 0.25 s for the numerical comparison. Two metrics were used for the error calculation: relative norm 1 ($\|E\|_1$) and relative norm 2 ($\|E\|_2$) given by:

$$\|E\|_1 = \frac{\sum_i^n |\phi_i^e - \phi_i^c|}{\sum_i^n |\phi_i^e|}, \tag{29}$$

Table 1
Study of the convergence of convective schemes, associated with an explicit Finite Volume Method.

Scheme	$N \times N$	$\|E\|_1$		$\|E\|_2$	
		Error	Order	Error	Order
FOU	17×17	0.336	–	0.315	–
	33×33	0.207	0.729	0.226	0.501
	65×65	0.126	0.733	0.153	0.579
	129×129	0.067	0.919	0.091	0.753
TOPUS	17×17	0.240	–	0.273	–
	33×33	0.114	1.117	0.168	0.732
	65×65	0.041	1.489	0.074	1.202
	129×129	0.014	1.564	0.029	1.346

$$\|E\|_2 = \sqrt{\frac{\sum_i^n (\phi_i^e - \phi_i^c)^2}{\sum_i^n (\phi_i^e)^2}} \tag{30}$$

where ϕ_i^e and ϕ_i^c are the "reference" and computational solutions at point i, respectively and n is the total number of nodes of the mesh. In Table 1, the convergence analysis of the numerical methods for the convective term is presented.

4.2. Implementation

The simulator is an in-house code implemented in C. Simulations were executed on an Intel(R) Core(TM) i7 3 GHz 8 Gb. The pseudocode can be seen in Algorithm 1.

Algorithm 1: Algorithm for the simulation of contrast dynamics during cardiac perfusion

```
Configurations of the model parameters
Calculate transmissibilities
Calculate pressure: while ||E_∞|| ≥ 10^-8 do
    Solve elliptic pressure equation
Calculate velocity; Choose Δt using CFL conditions; numIterations = time/Δt
for k ← 1 until numIterations do
    for each node (i, j) do
        Calculate Advection (adv_{i,j})
        Calculate Diffusion (dif_{i,j})
        Concentration: C^k_{i,j} = ((dif_{i,j} − adv_{i,j}) · Δt)/φ + C^{k−1}_{i,j}
    Update boundary conditions (Neumann and Dirichlet)
    Save data
```

5. Results and discussion

In this section we first present the comparison of TOPUS versus FOU numerical schemes. After this convergence analysis we perform simulations of the perfusion of contrast in the cardiac tissue for different scenarios: we consider the cases of isotropic and anisotropic perfusion as well as the presence or absence of an endocardial infarct.

5.1. TOPUS vs. FOU

Table 1 presents the results of the convergence analysis for the TOPUS and FOU schemes, both used to discretize the advective term of Eq. (8).

We can make the following observations about the two methods used here:

- As in [4–6], the TOPUS scheme is of higher order than the FOU scheme.
- The order of convergence of the FOU scheme is near linear, as expected.
- The order of the TOPUS scheme for this particular problem was between 1 and 2, i.e. around $O(h^{1.5})$.

After this comparison, all the next results were obtained using the TOPUS scheme to discretize the advective term of Eq. (8).

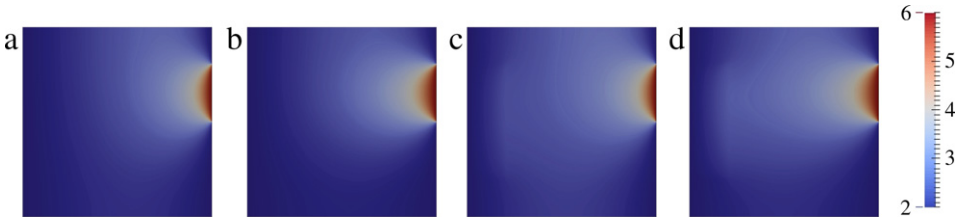

Fig. 7. Pressure field in cases (a) isotropic and non-infarcted, (b) anisotropic and non-infarcted, (c) isotropic and infarcted, (d) anisotropic and infarcted.

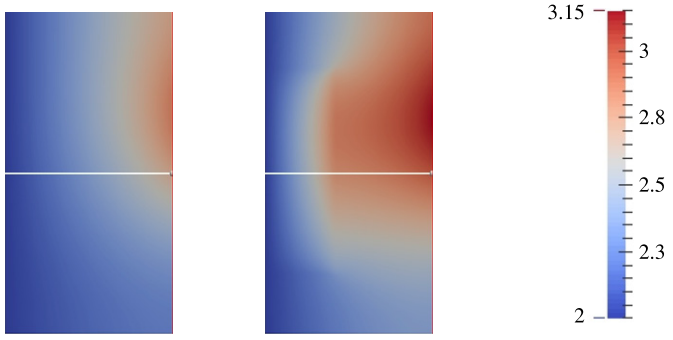

(a) Without in-farct. (b) Near an in-farct area. (c)

Fig. 8. Pressure distribution in the left side of the domain. Simulation of isotropic, non-infarct (a) and infarct (b) cases.

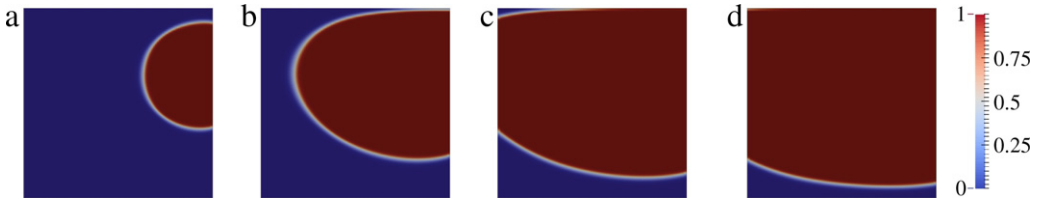

Fig. 9. Isotropic and non-infarcted simulation. Contrast distributions at: (a) 0.03 s; (b) 0.15 s; (c) 0.30 s; e (d) 0.45 s.

5.2. Simulated Scenarios of contrast perfusion in the heart

Fig. 7 presents the numerical solutions obtained for the pressure distribution for the four scenarios considered: isotropic and non-infarcted tissue simulation, anisotropic and non-infarcted tissue simulation, isotropic and infarcted tissue simulation and anisotropic and infarcted tissue simulation.

It is possible to observe the similarities between the four simulated scenarios. The contrast between the region near to Γ_{E2} and the other regions Γ_{E1}, Γ_{E3}, Γ_{west}, Γ_{north} and Γ_{south} is clear. The pressure in Γ_{E2} was assumed to be higher by considering that a coronary artery was near this region. Fig. 5 exemplified this situation.

Nevertheless, subtle differences exist among all the different simulations. For instance, Fig. 8 presents a zoom in the left part of the pressure results, comparing the cases with and without the infarct region for the isotropic case. Without the infarct region pressure distribution is smooth, whereas in the presence of an infarct area we observe an abrupt pressure decay or gradient.

Figs. 9–12 present the simulation results of the perfusion of contrast in the cardiac tissue for the four scenarios considered: isotropic and non-infarcted tissue simulation, anisotropic and non-infarcted tissue simulation, isotropic and infarcted tissue simulation and anisotropic and infarcted tissue simulation, respectively.

We observed that the model was able to detect non-infarcted regions in the myocardium, absence of non-perfused spots (Figs. 9 and 10) and infarcted regions, presence of a non-perfused spot in the infarcted area (Figs. 11 and 12). In addition we can observe that in the simulations that considered the diffusion and permeability to be isotropic the perfusion of contrast was faster in the horizontal direction than the simulations of an anisotropic tissue. Since it is known that the main pressure gradient at diastole is between epicardial and endocardial surfaces we note that the tissue main anisotropic direction, which is orthogonal to the pressure gradient (myocardial fibers run parallel to the surfaces), speeds up the perfusion in the cardiac tissue.

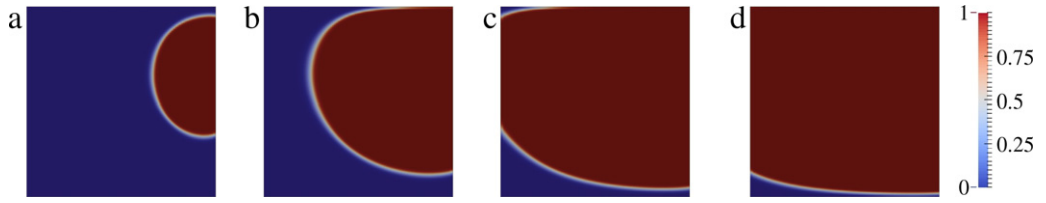

Fig. 10. Anisotropic and non-infarcted simulation. Contrast distributions at: (a) 0.03 s; (b) 0.15 s; (c) 0.30 s; e (d) 0.45 s.

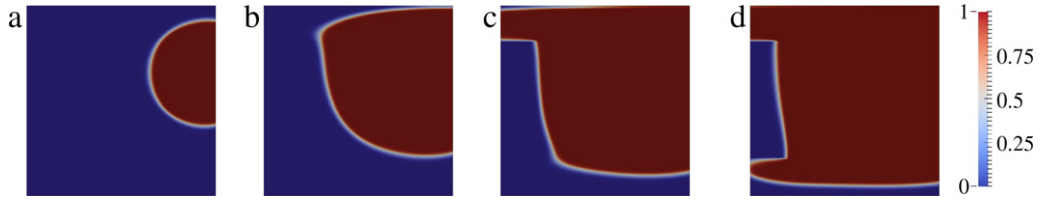

Fig. 11. Isotropic and infarcted simulation. Contrast distributions at: (a) 0.03 s; (b) 0.15 s; (c) 0.30 s; e (d) 0.45 s.

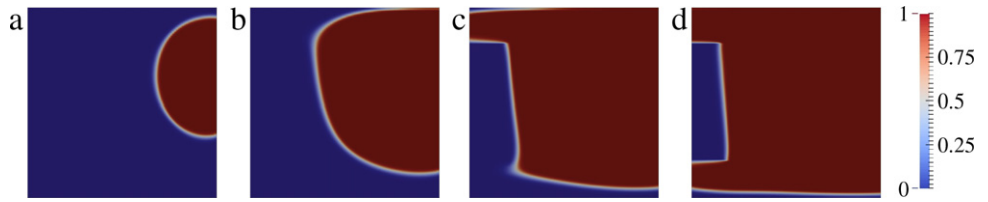

Fig. 12. Anisotropic and infarcted simulation. Contrast distributions at: (a) 0.03 s; (b) 0.15 s; (c) 0.30 s; e (d) 0.45 s.

Fig. 12(d) highlights the similarities between our simulation results and clinical images obtained by cardiac perfusion MRI exams based on contrast. Therefore, our model was able to qualitatively reproduce the perfusion of contrast in the heart.

5.3. Limitations

The experiments conducted here simulate the blood perfusion in myocardium with a contrast agent (gadolinium [7]). The parameters used here (porosity and permeability tensor of the media, diffusion tensor of gadolinium), the initial and boundary conditions are all in agreement with the reported values found in the literature. Nevertheless, it is reported that the intensity of the contrast (gadolinium) only reaches its peak after 9 s of cardiac perfusion [3]. In our simulations, this peak of intensity was achieved during a single diastole time-window, i.e. after 0.55 s.

This difference is due to the fact that during the clinical perfusion exam, gadolinium leaks to the extravascular medium. In fact, most of the brightness observed during a perfusion MRI exam is related to the accumulation of the contrast substance in the interstitial space [3]. As we mentioned before, in this work we have considered that perfusion was only taking place in the intravascular domain, i.e. our model used the same hypothesis as the model presented in [1]. It turned out that this assumption is the main limitation of our model. Therefore, we propose as future work the modeling of the adsorption phenomena to the extravascular media.

6. Conclusion and future work

We presented here a simplified model that describes the blood and contrast perfusion in a transmural wall of the left ventricle of the heart. The model was able to capture and identify regions with low permeability in the case of the simulations that considered a sub-epicardial infarct. Therefore, the simulation results are qualitatively in agreement with the expected phenomena, i.e. with the described images obtained by the non-invasive exams of cardiac perfusion MRI. However, this first model did not take into account the leak of gadolinium to the extravascular medium. This leak causes the signal strength of the contrast to grow slower than in our simulations. In the near future, we intend to improve the model based in porous media used here with a model that identifies this leak of gadolinium to the extravascular medium. In addition, improvements can be made in the numerical solution of the elliptic equation, such as the use of the multigrid method; and parallel computing techniques should be consider, since the simulation of each scenario took a considerable long time (approximately 60 min).

Acknowledgments

The authors would like to acknowledge the financial support provided by FAPEMIG, CAPES, UFJF, FINEP and CNPq.

References

[1] C. Michler, A.N. Cookson, R. Chabiniok, E. Hyde, J. Lee, M. Sinclair, T. Sochi, A. Goyal, G. Vigueras, D.A. Nordsletten, N.P. Smith, A computationally efficient framework for the simulation of cardiac perfusion using a multi-compartment Darcy porous-media flow model, Int. J. Numer. Methods Biomed. Eng. 29 (2013) 217–232.
[2] J. Huyghe, T. Arts, D.V. Campen, R. Reneman, Porous medium finite element model of the beating left ventricle, Am. J. Physiol. - Heart Circ. 262 (1992) 1256–1267.
[3] E. Nagel, C. Klein, I. Paetsch, S. Hettwer, B. Schnackenburg, L. Wegscheider, E. Fleck, Magnetic resonance perfusion measurements for the noninvasive detection of coronary artery disease, Circulation 108 (2003) 432–437.
[4] V. Ferreira, R. Queiroz, G. Lima, R. Cuenca, C. Oishi, J. Azevedo, S. Mckee, A bounded upwinding scheme for computing convection-dominated transport problems, Comput. Fluids 57 (2012) 208–224.
[5] V. Ferreira, R. de Queiroz, M. Candezano, G. Lima, L. Correa, C. Oishi, F. Santos, Simulation results and applications of an advection bounded scheme to practical flows, Comput. Appl. Math. 31 (2012) 591–616.
[6] R. de Queiroz, V. Ferreira, R. Cuenca, A new high resolution TVD scheme for unsteady flows with shock waves, Tend. Mat. Apl. Comput. 9 (2008) 311–320.
[7] M. Pop, N. Ghugre, L.M.V. Ramanan, G. Stanisz, A. Dick, G. Wright, Quantification of fibrosis in infarcted swine hearts by ex vivo late gadolinium-enhancement and diffusion-weighted MRI methods, Phys. Med. Biol. 58 (2013) 5009–5028.
[8] E. Isaacson, H.B. Keller, Analysis of Numerical Methods, John Wiley and Sons, United States, 1966.
[9] M.H. Holmes, Introduction to Numerical Methods in Differential Equations, Springer, United States, 2007.